

Work function modulation of graphene with binary mixture of Cu and C₆₀F₃₆



ChenQiang Hua^{a, b}, SiHan Zhou^a, ChunWei Zhou^a, WeiDong Dou^c, HongNian Li^b, YunHao Lu^{b, **}, JianQiang Zhong^a, HongYing Mao^{a, *}

^a Department of Physics, Hangzhou Normal University, Hangzhou, 310036, China

^b Department of Physics, Zhejiang University, Hangzhou, 310036, China

^c Laboratory of Low-dimensional Carbon Materials, Physics Department, Shaoxing University, Shaoxing, 312000, China

ARTICLE INFO

Article history:

Received 21 January 2021

Received in revised form

18 March 2021

Accepted 4 April 2021

Available online 13 April 2021

Keywords:

Graphene

Work function

Binary mixture

Surface dipole

ABSTRACT

Graphene is a promising candidate for flexible, transparent electrodes in organic electronic devices. In order to achieve enhanced device performance, work function (WF) modulation of graphene for better electric contact at the electrode/active materials interface is of significant importance. Herein, we have demonstrated the effective modulation of graphene WF with binary mixture of Cu and C₆₀F₃₆ and the highest WF of ~6.04 eV is obtained after *in situ* thermal annealing at 150 °C. The ultraviolet photoelectron spectroscopy (UPS) and X-ray photoelectron spectroscopy (XPS) measurement indicate that the growth of Cu on C₆₀F₃₆-modified graphene leads to C–F bonds breaking of C₆₀F₃₆ and the formation of Cu–F bonds on the basal plane of graphene, which is responsible for the large WF increase of graphene. The mechanism for the WF increase of binary mixture of Cu and C₆₀F₃₆ modified graphene (BMG) has been corroborated by density-functional theoretical (DFT) calculations, which shows that the C–F bond breaking of C₆₀F₃₆ is facilitated by Cu adatoms, and the WF increase can be attributed to the formation of surface dipole layer with the direction pointing from vacuum to graphene, which is consistent with UPS and XPS results. Moreover, our results indicate that other 3d transition metal adatoms (Ti, V, Fe, Co, and Ni) on graphene can also facilitate the C–F bond breaking of C₆₀F₃₆ and the formation of surface dipole layer, resulting in the WF increase of graphene.

© 2021 Elsevier Ltd. All rights reserved.

1. Introduction

Graphene, a single atomic layer arranged by *sp*² hybridized carbon atoms, has attracted extensive research attentions since its first experimental isolation in 2004 [1]. Because of its peculiar structural characteristics, unique physical and chemical properties have been demonstrated including unprecedented high carrier mobility, half-integer quantum Hall effect, superlative mechanical strength, and incomparable thermal conductivity [2–6]. With the great progress in the synthesis of high-quality graphene on a large scale [7–10], its applications in organic electronic devices [11,12], chemical sensors [13,14], supercapacitors [15], and drug delivery [16] have been extensively explored in the last decade.

For its applications in organic electronic devices, graphene is

regarded as a promising alternative to highly conductive indium tin oxide (ITO) for flexible, transparent electrodes [9,17]. Even though organic photovoltaic cells (OPVs) and light emitting diodes (OLEDs) have been successfully fabricated using graphene as transparent electrodes, graphene-based devices always suffer from poor performance compared to their counterparts using ITO as transparent electrodes [18–20]. There are two major disadvantages for graphene-based devices: i) high sheet resistance (200–300 Ω sq⁻¹) as compared to the ITO (10–30 Ω sq⁻¹); ii) relatively low work function (~4.4 eV) than that of ITO (~4.8 eV). Synthesis of graphene/metal nanowire composite films is an effective method to reduce the sheet resistance of graphene-based transparent electrodes. The sheet resistance can be as low as 13.7 Ω sq⁻¹ with high transmittance for silver nanowire and graphene hybrid-based electrodes [21]. Doping is another method to improve the charge carrier concentration and electrical conductivity, and hence decrease the sheet resistance of graphene. On the other hand, work function (WF) optimization is still critical for the enhanced devices

* Corresponding author.

** Corresponding author.

E-mail addresses: luyh@zju.edu.cn (Y. Lu), phymaohy@hznu.edu.cn (H. Mao).

performance by matching the energy levels between graphene and active layers in electronic devices [22–30]. For example, when graphene is used as the anode in OPVs, the WF of graphene need to be further increased to match with the highest occupied molecular orbital (HOMO) of donor-type organic molecules in OPVs, which facilitates the efficient hole collection at the electrode. As the WF is related to the energy difference between vacuum level (E_v) and Fermi level (E_f), various approaches, including electrostatic gating, chemical and optical doping, have been developed to shift the E_f of graphene to obtain a desired WF value [31–36].

In the present study, we report an efficient way to modulate the WF of graphene by the co-adsorption of $C_{60}F_{36}$ molecules and Cu adatoms. After the surface modification of graphene by $C_{60}F_{36}$, the WF of graphene increases from 4.40 to 5.32 eV. This is attributed to charge transfer from graphene to $C_{60}F_{36}$ resulting in a p-type doping in graphene, which downward shifts E_f of graphene and hence increases its WF. More importantly, the WF can be further increased by the sequential deposition of Cu adatoms onto the $C_{60}F_{36}$ modified graphene. The highest WF of 6.04 eV is obtained after *in situ* annealing of BMG at 150 °C. Combining the ultraviolet photoelectron spectroscopy (UPS), X-ray photoelectron spectroscopy (XPS) and density-functional theoretical (DFT) calculations, it is revealed that Cu adatoms can facilitate the breaking of the C–F bonds in $C_{60}F_{36}$ and the formation of interfacial dipole layer (Cu–F) is responsible for the WF increase. This mechanism is general for the transition metal (TM) adatoms other than Cu and the effective WF increase can be also realized by depositing them (e.g. Ti, V, Fe, Co, Ni) on $C_{60}F_{36}$ modified graphene, which is validated by UPS/XPS measurements and DFT calculations.

2. Material and methods

2.1. Growth of graphene

A custom designed low-pressure chemical vapor deposition (LPCVD) system has been used for the growth of graphene on copper foil [37]. A mixture gas of Ar, H_2 and O_2 was introduced into the LPCVD chamber after pumping down to a base pressure of 0.01 Pa. During the growth, flow rates of Ar and H_2 were kept at 600 sccm and 100 sccm. The flow rate of O_2 ranged from 0 to 0.1 sccm depending on different growth stages. Before the growth of graphene, copper foil underwent 1050 °C thermal treatment for 1 h for better crystallinity. During the growth of graphene, 0.5 sccm methane was introduced into the LPCVD chamber. The growth period lasted for 1 h to obtain high quality and large-scale graphene sample. After the growth, the system was cooled down to RT. Graphene samples were then transferred to SiO_2 substrates (Si wafer with a thin layer of native oxide) for UPS and XPS measurements by wet-transfer method using poly(methyl methacrylate) (PMMA). Wrinkles are observed in the optical microscope and atomic force microscope (AFM) images (Fig. S1a and S1b) which are the characteristic phenomenon of transferred graphene. The Raman spectrum (Fig. S1c) shows the characteristic vibrational peaks at $\sim 1585\text{ cm}^{-1}$ and 2688 cm^{-1} corresponding to G and 2D peak of graphene, respectively. The peak intensity of 2D peak is 2 times larger than that of G peak, indicating the single layer nature of our graphene sample. Moreover, the nearly undetectable D peak at $\sim 1350\text{ cm}^{-1}$ manifests the defect-free property of the transferred graphene sample.

2.2. Characterizations

Our *in situ* UPS and XPS measurements were performed in a multifunctional ultrahigh vacuum (UHV) VT-SPM system (Omicron Instruments) with a base pressure better than 3×10^{-10} mbar in the

analysis chamber. He I (21.2 eV) is the excitation source for UPS measurements, and a -5 V bias was applied to sample for WF measurements. An Al $K\alpha$ source ($h\nu = 1486.7\text{ eV}$) is used for XPS measurements. Before the deposition of $C_{60}F_{36}$, thoroughly degassing was carried out overnight. The deposition rate for $C_{60}F_{36}$ was kept at 0.2 nm/min which was calibrated by a quartz-crystal-microbalance (QCM) as well as from the attenuation of Si 2p peak after the deposition of $C_{60}F_{36}$. Cu was thermally deposited onto $C_{60}F_{36}$ modified graphene using a medium temperature effusion cell at 980 °C with the deposition rate of 0.1 nm/min. A Zeiss Axio optical microscope and AFM (Bruker multimode 8) with a tapping-mode were used to obtain optical microscope and AFM images of graphene samples. The Raman spectrum was carried out using a Horiba HR Evolution Raman spectrometer with laser excitation of 532 nm.

2.3. DFT calculations

Our first-principle calculations were performed using Vienna ab initio package [38]. The projector-augmented wave (PAW) pseudo-potential were used with the generalized gradient approximation of Perdew, Burke, and Ernzerhof (PBE) to the exchange–correlation functional [39,40]. We optimized pristine graphene structure firstly and then fix the lattice constants when adsorbing adatoms. The force criteria were set to 0.01 eV/Å. Besides, a 10^{-5} eV of energy convergence threshold was adopted in both optimization and energy calculations. For adsorption calculations, the van der Waals correction D2 method of Grimme was added [41]. To avoid the interaction between periodic counterparts, in all the models, we built at least 20 Å vacuum, which is perpendicular to the graphene plane. Here, the energy cutoff was set to 450 eV and $9 \times 9 \times 1$ k -points were utilized to mesh Brillouin zone of $5 \times 5 \times 1$ graphene supercell. The differential charge density is defined as follows:

$$\Delta\rho_{dcd} = \rho_{total} - \sum_i \rho_i$$

where ρ_{total} is the total charge density and ρ_i is the charge density for separate graphene, Cu adatom and F atom.

3. Results and discussion

The WF modulation of BMG is investigated using *in situ* UPS measurements. Fig. 1a and b shows UPS spectra at the secondary electron cutoff and valence band region for pristine graphene, 2.0 nm $C_{60}F_{36}$ on graphene, and 2.0 nm Cu on $C_{60}F_{36}$ /graphene, respectively. The WF for pristine graphene is 4.40 eV, which is in good agreement with previous reports [42]. A WF increase of 0.92 eV is observed when 2.0 nm $C_{60}F_{36}$ is used to modify the pristine graphene, which can be understood with the surface charge transfer induced p-type doping in graphene [43]. As we known, $C_{60}F_{36}$ is an efficient p-dopant due to its high electron affinity ($\sim 5.0\text{ eV}$) [44], spontaneous electron transfer from graphene to $C_{60}F_{36}$ occurs upon the deposition of $C_{60}F_{36}$ on graphene, leading to the formation of electron depletion layer in graphene. Consequently, downward shift of the graphene Fermi level is arisen. More interestingly, the WF of $C_{60}F_{36}$ /graphene further increases to 5.74 eV with the sequential growth of 2.0 nm Cu, corresponding to a total increase of 1.34 eV in WF as compared to the pristine graphene. Previous results have demonstrated that the WF of Cu ranged from 4.40 to 4.94 eV depending on the different crystal planes [45,46]. Considering that the WF of $C_{60}F_{36}$ /graphene is 5.32 eV which is higher than that of Cu, therefore, the further WF increasement after Cu deposition cannot be attributed to the surface charge transfer induced p-type doping.

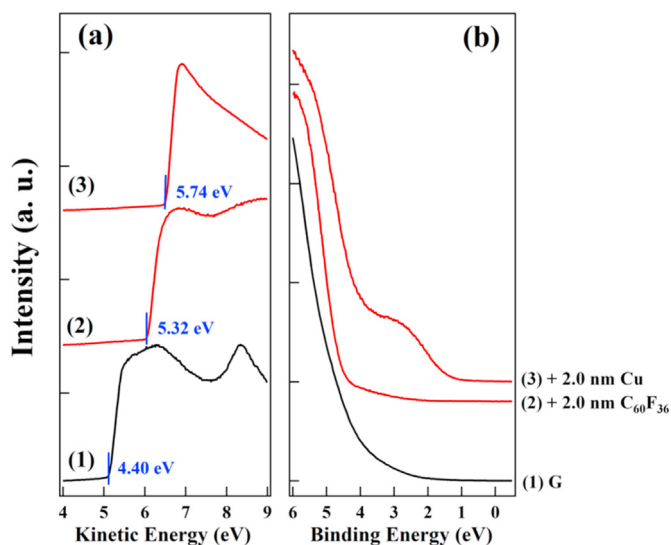


Fig. 1. UPS spectra at the (a) secondary electron cutoff and (b) valence band region for pristine graphene (1), 2.0 nm C₆₀F₃₆ on graphene (2), and 2.0 nm Cu on C₆₀F₃₆/graphene (3), respectively. (A colour version of this figure can be viewed online.)

In order to reveal the mechanism for the WF increase after the deposition of Cu on C₆₀F₃₆/graphene, XPS measurements have been

carried out. Fig. 2a shows XPS spectra of C 1s after the sequential deposition of Cu and C₆₀F₃₆ on graphene. For the pristine graphene, a single C 1s peak is observed at 284.3 eV. After the growth of 2.0 nm C₆₀F₃₆, there are three peaks in the C 1s region. The peak at 284.1 eV derives from sp² hybridized carbon atoms in graphene. The ~0.2 eV shift of graphene related C 1s peak to lower binding energy part corroborates the surface transfer p-type doping of graphene after C₆₀F₃₆ modification. The downward shift of graphene Fermi level leads to the upward shift of graphene related C 1s peak. The other two peaks locating at 286.0 and 288.3 eV are attributed to carbon atoms from C–C bonds and C–F bonds in C₆₀F₃₆, respectively [47]. Table 1 summarizes the C 1s, F 1s, and Cu 2p peak fittings for BMG before and after thermal annealing. With the sequential deposition of 2.0 nm Cu, the peak intensity ratio between carbon atoms from I_{(C–F)bonds} and I_{(C–C)bonds} in C₆₀F₃₆ decreases from ~1.47 (C₆₀F₃₆/graphene) to ~0.87 (Cu on C₆₀F₃₆/graphene), indicating the decomposition of C₆₀F₃₆ molecules. Bond breaking of C–F occurs upon the deposition of Cu on C₆₀F₃₆ modified graphene. Fig. 2b shows XPS spectra of F 1s after the sequential deposition of Cu and C₆₀F₃₆ on graphene. A single F 1s peak locating at 686.9 eV is observed on C₆₀F₃₆/graphene, which is assigned to F atoms in F–C bonds of C₆₀F₃₆. After the sequential deposition of 2.0 nm Cu, a notable peak broadening of the F 1s peak is observed, and a new feature locating at the lower binding energy part emerges. This new feature locating at 684.4 eV is attributed to F atoms in the metal fluoride, and the intensity ratio between F atoms from I_{(F–C)bonds} of C₆₀F₃₆ and I_(F–Cu) bonds of copper fluoride

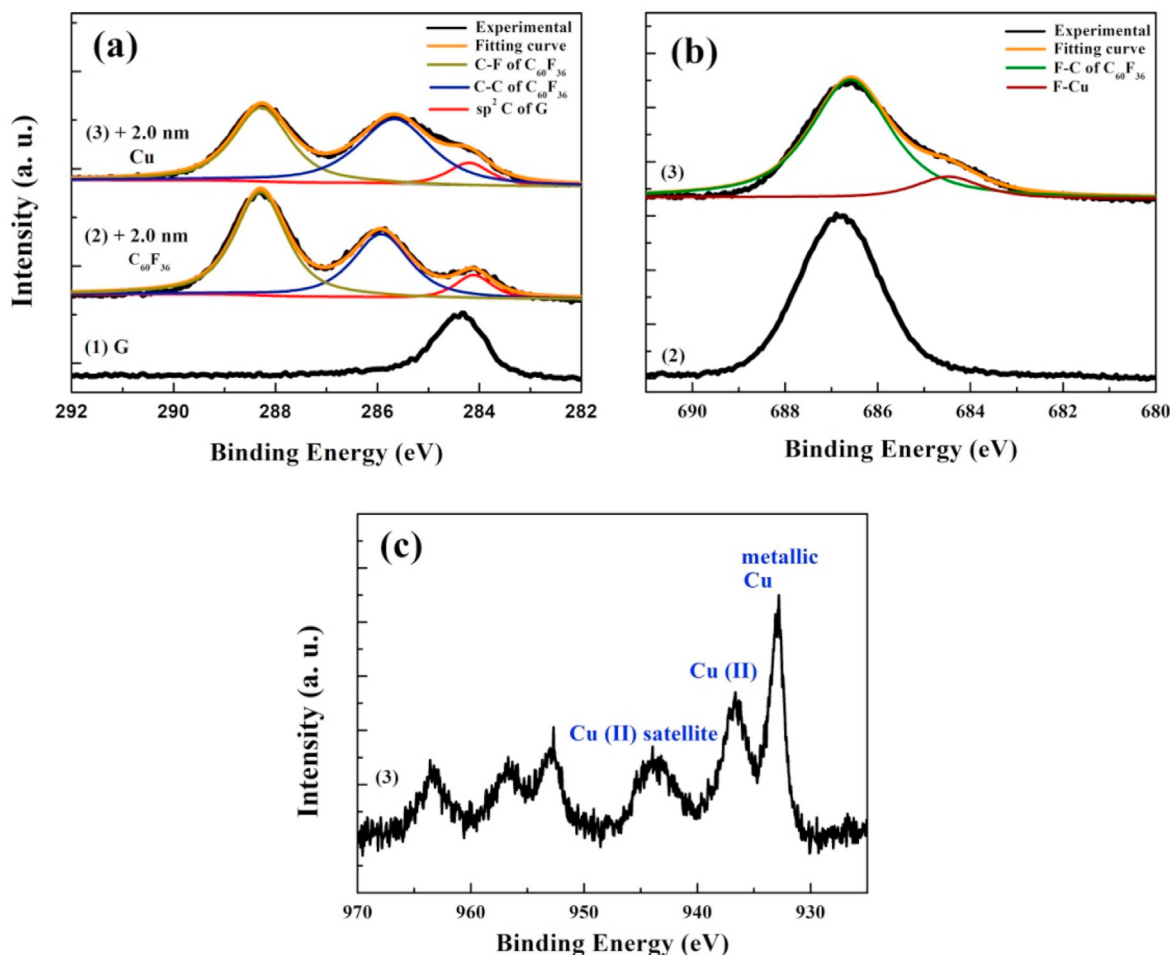


Fig. 2. XPS spectra of (a) C 1s, (b) F 1s, and (c) Cu 2p after the sequential deposition of Cu and C₆₀F₃₆ on graphene. (A colour version of this figure can be viewed online.)

Table 1
Summary of C 1s, F 1s and Cu 2p peak fittings for BMG before and after thermal annealing.

Samples	Peak intensity (a. u.)						
	C 1s			F 1s		Cu 2p _{3/2}	
	C–F of C ₆₀ F ₃₆	C–C of C ₆₀ F ₃₆	sp ² C of G	F–C of C ₆₀ F ₃₆	F–Cu	Cu–F	Metallic Cu
Graphene			5269				
+2.0 nm C ₆₀ F ₃₆	9113	6194	1533	50735			
+2.0 nm Cu	7141	8165	1724	42446	6465	11570	12412
Anneal @100 °C	6833	8489	1956	40887	7003	14367	8704
Anneal @150 °C	5923	7511	2591	24629	7445	14192	8968
Anneal @200 °C	2279	5754	4332	16965	5272	9754	13770
Anneal @300 °C	1036	2751	4984	2114	4729	7072	14398

is ~6.57. The existence of copper fluoride after the deposition of Cu on C₆₀F₃₆/graphene is also corroborated by the XPS spectrum of Cu 2p as shown in Fig. 2c. The peak doublet of the Cu 2p_{3/2} and 2p_{1/2} component locating at 933.1 and 953.0 eV is attributed to metallic Cu, while the peak doublet at 936.9 and 956.8 eV derives from Cu (II) species coordinated to F. The other peak doublet centered at 943.8 and 963.2 eV corresponds to the shake-up satellites for Cu (II) [48–50]. The appearance of Cu (II) species suggests that F atoms are likely to be chemically bonded to Cu atoms after breaking F–C bonds. Considering the high electronegativity of F atoms, the formation of F–Cu bonds lead to an interface dipole moment pointing to the substrate, and hence the increased WF after the sequential deposition of Cu on C₆₀F₃₆ modified graphene [24,25].

Moreover, we investigate the thermal stability of the BMG after *in situ* annealing. Fig. 3a displays UPS spectra at the secondary

electron cutoff region for the BMG after *in situ* thermal annealing. The highest WF of 6.04 eV is obtained with thermal annealing at 150 °C. The schematic illustration of WF modulation of graphene with binary mixture of Cu and C₆₀F₃₆ before and after thermal annealing is shown in Fig. S2. As compared to other chemical doping methods [51,52], our approach obtains the largest WF increase (~1.64 eV), which is caused by the simultaneously surface charge transfer induced p-type doping as well as the formation of Cu–F species at the surface of BMG. It has to be noted that the high WF of 6.04 eV results from the co-adsorption Cu and C₆₀F₃₆. As shown in Fig. S3, the WF increases to 5.40 and 5.48 eV for 5.0 and 10.0 nm C₆₀F₃₆ modified graphene, which is much lower than that of BMG. Moreover, the BMG possesses relatively good air stability since long-term stability is essential for its application in OPVs. As shown in Fig. S4, the WF of BMG slightly decreases to 5.94 and

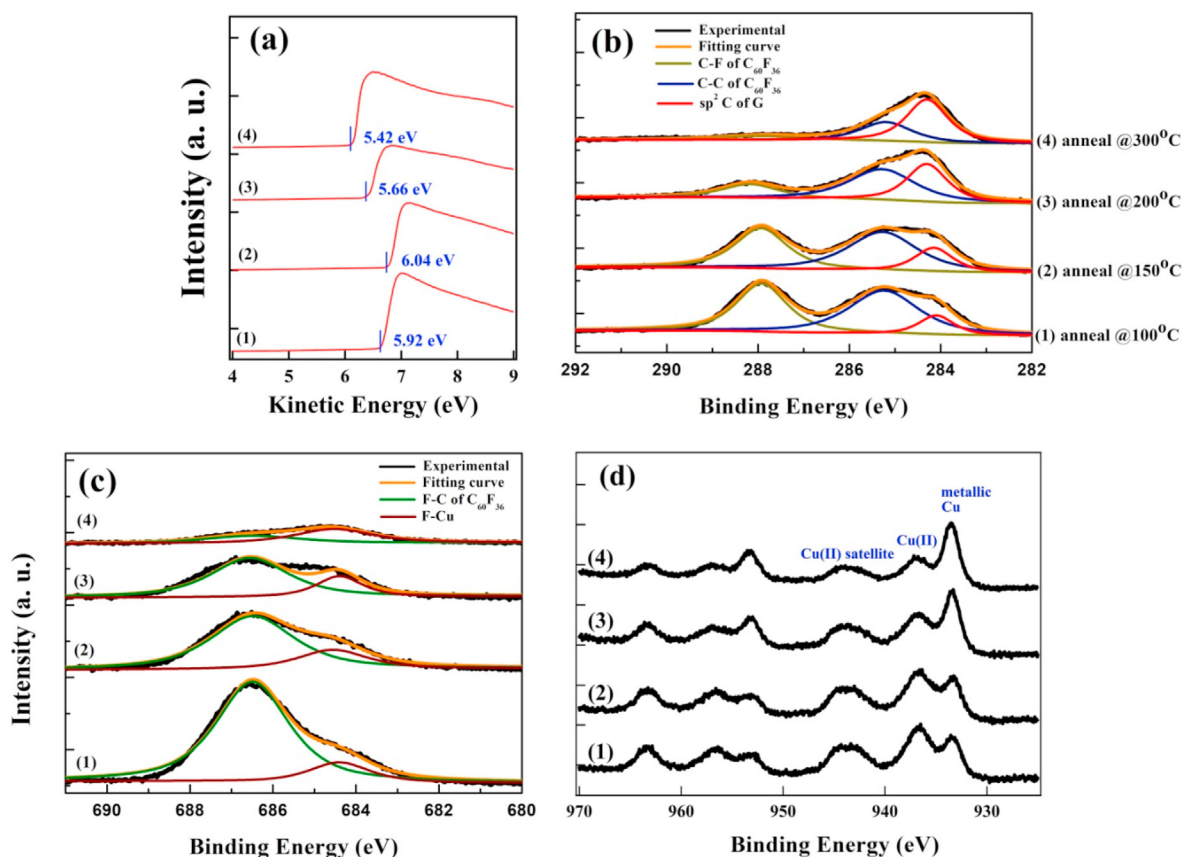


Fig. 3. UPS spectra at the (a) secondary electron cutoff and XPS spectra of (b) C 1s, (c) F 1s, and (d) Cu 2p for BMG after *in situ* thermal annealing. (A colour version of this figure can be viewed online.)

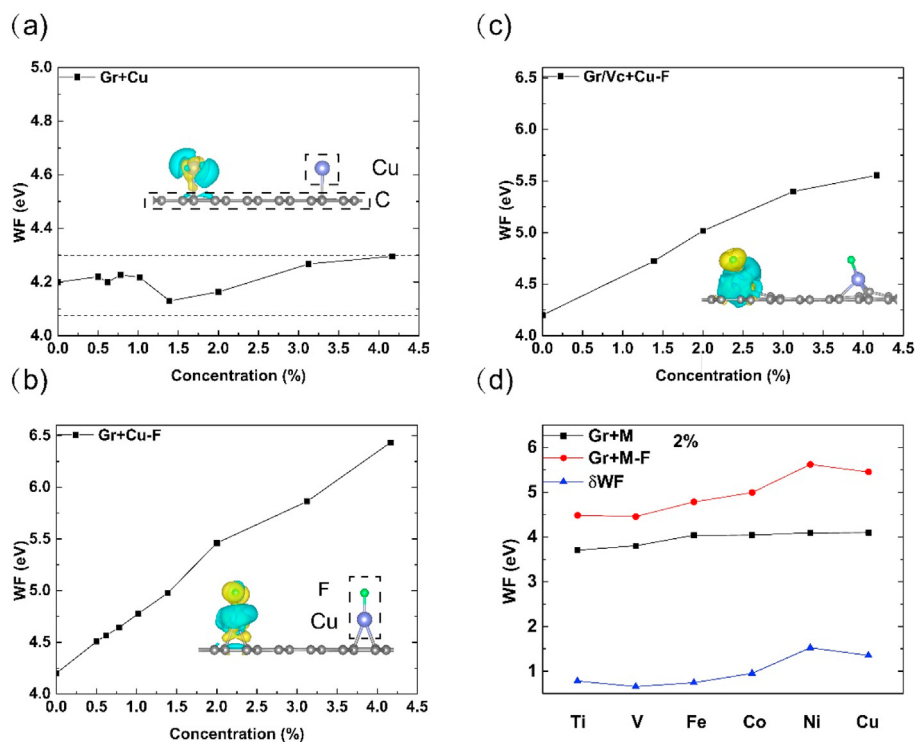


Fig. 4. Coverage-dependent Work function of (a) only Cu adatom on perfect graphene, (b) Cu–F binary dipole layer on perfect graphene and (c) defected graphene with carbon vacancy. The insets show differential charge density, where yellow and blue represent electron accumulation and depletion region, respectively. Isosurface is 0.005 Bohr^{-3} . (d) Work function of only TM (red-dot line) and TM-F binary (black-square line) adsorbed on perfect graphene. The increase of WF for each TM is plotted in blue-triangle line. (A colour version of this figure can be viewed online.)

5.86 eV after exposure to air for 1 h and 1 day, respectively. The WF decrease can be attributed to the possible oxidation of Cu in air. However, the WF for CuO ($\sim 5.90 \text{ eV}$) is still higher than that of graphene or $\text{C}_{60}\text{F}_{36}$ [53]. As a result, only slightly WF decrease of BMG is observed after air exposure. After thermal annealing to 200°C and 300°C , the WF of BMG decreases to 5.66 and 5.42 eV, respectively. As shown in Fig. 3b and Table 1, in spite of the decreased peak intensity, the C 1s peak intensity ratio between $I_{(\text{C}-\text{F})\text{bonds}}$ and $I_{(\text{C}-\text{C})\text{bonds}}$ decreases to ~ 0.80 and 0.79 when the annealing temperature is 100°C and 150°C , respectively. At higher annealing temperature, the decrease of C 1s peak intensity ratio between $I_{(\text{C}-\text{F})\text{bonds}}$ and $I_{(\text{C}-\text{C})\text{bonds}}$ becomes more pronounced, and it decreases to ~ 0.40 and 0.38 at 200°C and 300°C , respectively. This indicates that the bond breaking of C–F of $\text{C}_{60}\text{F}_{36}$ along with the desorption of $\text{C}_{60}\text{F}_{36}$ occur when the annealing temperature is higher than 150°C . Meanwhile, the intensity ratio between $I_{(\text{F}-\text{C})\text{bonds}}$ of $\text{C}_{60}\text{F}_{36}$ and $I_{(\text{F}-\text{Cu})\text{bonds}}$ of copper fluoride decreases after thermal annealing as revealing by F 1s XPS spectra shown in Fig. 3c. On the other hand, the peak intensity of F 1s from F–Cu bonds of copper fluoride reaches to its maximum value at 150°C as shown in Table 1, which indicates that the formation of F–Cu bond is facilitated at 150°C . When the annealing temperature increases to 200°C and 300°C , $I_{(\text{F}-\text{C})\text{bonds}}$ of $\text{C}_{60}\text{F}_{36}$ decreases significantly, deriving from bonds breaking of F–C bonds of $\text{C}_{60}\text{F}_{36}$ and the desorption of $\text{C}_{60}\text{F}_{36}$. Meanwhile, $I_{(\text{F}-\text{Cu})\text{bonds}}$ of copper fluoride also decreases, leading to the decreased WF of BMG at higher annealing temperature. In the case of Cu 2p peak (Fig. 3d and Fig. S5), the intensity ratio between Cu (II) species coordinated to F and metallic Cu increases from ~ 0.93 to ~ 1.65 and 1.58 when the annealing temperature increases to 100°C and 150°C , respectively. When we further increase the annealing temperature, the peak intensity from metallic Cu increases along with a gradual

attenuation of peak intensity from Cu (II) species, which indicate the thermal reduction of Cu (II) species to metallic Cu at higher annealing temperature. The intensity ratio between $I_{(\text{F}-\text{C})\text{bonds}}$ and $I_{(\text{F}-\text{Cu})\text{bonds}}$ decreases to ~ 0.71 and 0.49 at 200°C and 300°C , respectively. When the annealing temperature increases to 450°C , all Cu (II) species have been reduced (Fig. S6). During the thermal annealing process, Cu adatoms are of vital importance in promoting the bond breaking of C–F and formation of Cu (II) species coordinated to F. A controlled experiment has been carried out to confirm this hypothesis. As shown in Fig. S7, $2.0 \text{ nm C}_{60}\text{F}_{36}$ is deposited on graphene without the further growth of Cu adatoms. After *in situ* thermal annealing at 100°C , the C 1s peak intensity ratio between $I_{(\text{C}-\text{F})\text{bonds}}$ and $I_{(\text{C}-\text{C})\text{bonds}}$ of $\text{C}_{60}\text{F}_{36}$ remain intact (from ~ 1.46 to 1.44). This is obviously different from that of BMG, for which the C 1s peak intensity ratio between $I_{(\text{C}-\text{F})\text{bonds}}$ and $I_{(\text{C}-\text{C})\text{bonds}}$ of $\text{C}_{60}\text{F}_{36}$ decreases from ~ 1.47 to 0.80 after thermal annealing at 100°C . Moreover, the peak intensity of F 1s also shows a gradual attenuation with the increasing annealing temperature, but there is no appearance of new feature such as F atoms in the metal fluoride. Moreover, the sheet resistance of pristine graphene and BMG after thermal annealing at 150°C has been measured by 4 point probe method. The sheet resistance of pristine graphene decreases from $\sim 625 \Omega \text{ sq}^{-1}$ to $550 \Omega \text{ sq}^{-1}$ after surface functionalization with binary mixture of Cu and $\text{C}_{60}\text{F}_{36}$. The decreased sheet resistance of BMG is attributed to the increased hole concentration without the sacrifice of hole mobility within graphene which is also observed for the improved conductivity of CVD graphene after MoO_3 modification [54].

In order to reveal the origin of WF increasement after Cu deposition on $\text{C}_{60}\text{F}_{36}$ /graphene, DFT calculations have also been carried out. The calculated WF of pristine graphene is $\sim 4.2 \text{ eV}$, which is in agreement with previous results and the experimental

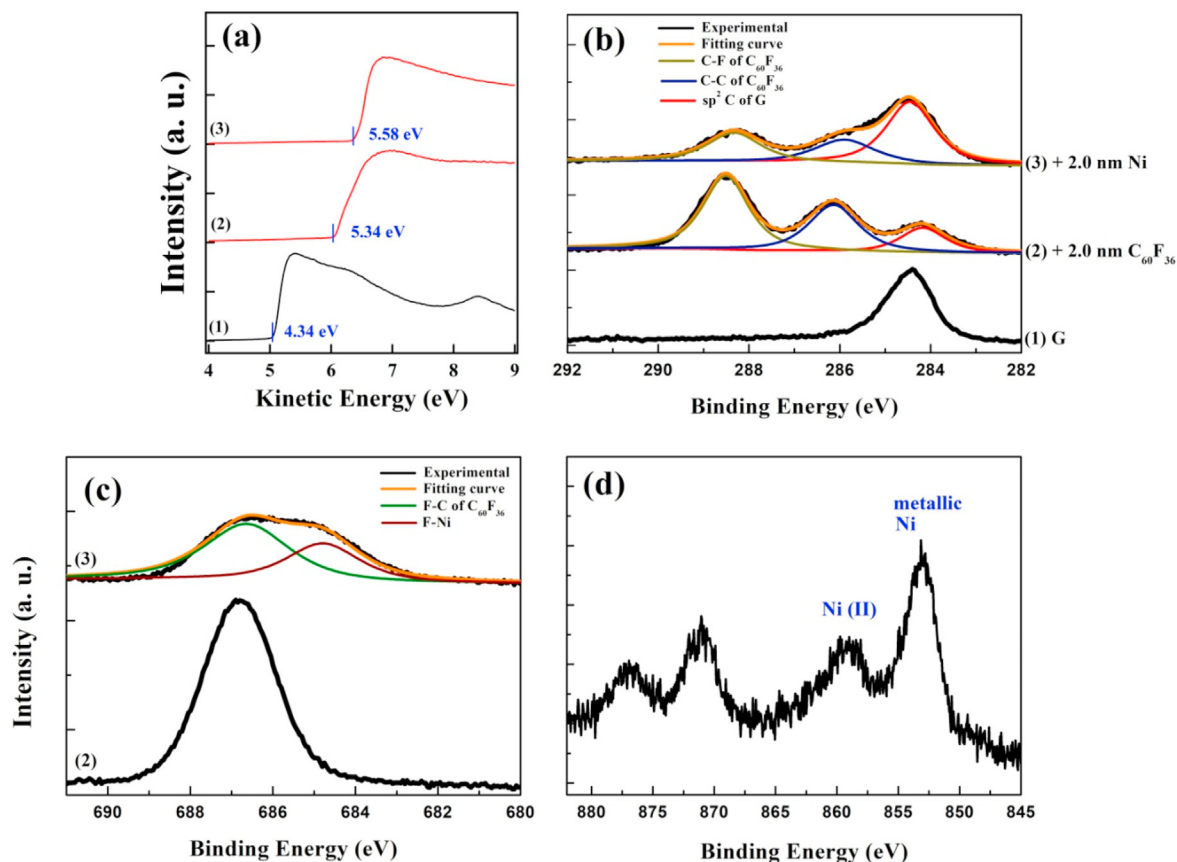


Fig. 5. UPS spectra at the (a) secondary electron cutoff and XPS spectra of (b) C 1s, (c) F 1s, and (d) Ni 2p after the sequential deposition of $C_{60}F_{36}$ and Ni on graphene. (A colour version of this figure can be viewed online.)

measurements (4.4 eV) [55]. It is noted that the variation of graphene WF after Cu modification is within 0.2 eV (Fig. 4a), which would not account for the large WF increase (~ 1.34 eV) for the BMG. The aforementioned XPS results of F 1s and Cu 2p indicate that some F atoms are bonding with Cu adatoms on the basal plane of graphene after the breaking of F–C bonds. It is found that the on-top position is the most favorable for Cu–F binary with Cu adatom binding on carbon atoms (Fig. 4b, and Fig. S8). As shown in Fig. 4b, only 2% coverage of Cu–F binary on graphene can increase the WF to 5.45 eV (~ 1.25 eV higher than that of pristine graphene). Furthermore, the WF can be further increased to higher than 6.0 eV when the coverage of Cu–F binary is larger than 3.2%. This is consistent with the increase of WF when the annealing temperature is lower than 150 °C. Such large increase of WF is quite related to the special adsorption geometry of Cu–F binary. Because of the large difference of electron affinity between Cu and F atom, electrons deplete on Cu adatoms (also graphene) and accumulate on F atoms. Consequently, a dipole forms on the graphene plane with the direction pointing from vacuum to graphene. Since all Cu–F binary has the same adsorption structure on graphene, they could assemble into a surface dipole layer with uniform dipole direction, which is responsible for the largely increased WF of BMG. Moreover, the effect of this surface dipole layer is robust against the defect of graphene because it is mainly caused by the charge transfer between Cu and F atoms, not graphene itself. Thus, the relationship between the WF and the coverage of adatoms are remained for the defected graphene with carbon vacancies (popular for the LPCVD grown graphene), although the WF is somehow a little lower than that of perfect graphene for all coverage due to

the screening of redundant electron around vacancy (Fig. 4c). Considering other possible structures for the Gr–Cu–F complex, we have also tested many Gr–Cu–F configurations (shown in Fig. S9), including Cu–2F (two fluorine atoms bonded to one copper atom), Cu–F bonded to Di VC (di-vacancy), and Cu–2F bonded to Di VC. After fully relaxation in calculation, it is found that the structure shown in Fig. 4b (Gr–Cu–F) is the most stable one with the formation energy of -2.63 eV, which is much larger than the thermal energy. Thus, this structure is stable under experimental condition. In addition, the WF increase of all these Gr–Cu–F configurations has also been confirmed as compared to that of pristine graphene which is shown in Fig. S9b. We further investigate the WF modulation of graphene with other 3d-TM adatoms on $C_{60}F_{36}$ modified graphene. The results are summarized in Fig. 4d for almost all 3d-TM adatoms. Due to the similar adsorption geometry of TM–F binary on graphene, the surface dipole layer can also form and the WF of BMG increases by ~ 1.0 eV comparing with the ~ 4.2 eV WF without surface modification.

In order to corroborate our conclusions from DFT calculations, the WF modulation of graphene with binary mixture of Ni and $C_{60}F_{36}$ has also been investigated in experiment. As shown in Fig. 5a, the WF of $C_{60}F_{36}$ modified graphene increases from 5.34 to 5.58 eV after the deposition of 2.0 nm Ni, and it can further increase to 5.70 eV with thermal annealing at 150 °C (Fig. S10a). Similar to the binary mixture of Cu and $C_{60}F_{36}$, the adsorption of Ni adatoms results in the bond breaking of C–F and formation of Ni (II) species coordinated to F. The bond breaking of C–F is evidenced by the decreased intensity ratio between C 1s peak of carbon atoms from C–F and those from C–C after the growth of Ni (Fig. 5b and

Table S1). As represented in Fig. 5c and d, a new F 1s feature emerges at the lower binding energy part which is attributed to F atoms in the metal fluoride. We can also observe the appearance of Ni 2p peak doublet at 859.3 and 877.0 eV deriving from Ni (II) species coordinated to F [56]. The effects of thermal annealing on binary mixture of Ni and C₆₀F₃₆ modified graphene are shown in Fig. S10. The WF increases with mild thermal annealing but decreases when the annealing temperature is higher than 150 °C. When the annealing temperature increases to 300 °C, the F 1s peak is dominated by the component from nickel fluoride.

4. Conclusions

The WF modulation of graphene has been realized by surface modification with binary mixture of Cu and C₆₀F₃₆. The highest WF increase of 1.64 eV (from -4.40 to 6.04 eV) is obtained after *in situ* thermal annealing at 150 °C. On the basis of our UPS and XPS results, spontaneous electron transfer from graphene to C₆₀F₃₆ occurs at the interface, leading to the downward shift of graphene Fermi level and the increased WF. The sequential deposition of Cu on C₆₀F₃₆ modified graphene results in C–F bonds breaking of C₆₀F₃₆ and formation of Cu–F binary on the basal plane of graphene facilitated by *in situ* thermal annealing at an optimized temperature, which is responsible for the further WF increase of BMG. In addition, our DFT results confirm the C–F bond breaking mechanism of C₆₀F₃₆ by Cu adatoms and the formation of interface dipole layer which is consistent with our UPS as well as XPS results. Moreover, our DFT calculations show that other 3d-TM adatoms, including Ti, V, Fe, Co, and Ni, can also facilitate the C–F bond breaking of C₆₀F₃₆ and the formation of metal-F binary on graphene, leading to the WF increase with binary mixture of metal and C₆₀F₃₆ modified graphene. It should be noted that the TM adatoms are not only the part of dipole layer, but also catalyst facilitating the C–F bond breaking of C₆₀F₃₆. Our findings promise a new interfacial engineering approach to modulate the WF of graphene and pave the way towards its potential applications in optoelectronic devices.

CRediT authorship contribution statement

ChenQiang Hua: Investigation, Data curation, Formal analysis, Writing – original draft. **SiHan Zhou:** Investigation, Formal analysis, Software. **ChunWei Zhou:** Data curation, Formal analysis. **Weidong Dou:** Data curation, Resources, Funding acquisition. **HongNian Li:** Formal analysis, Writing – review & editing. **YunHao Lu:** Formal analysis, Resources, Funding acquisition, Writing – review & editing. **JianQiang Zhong:** Funding acquisition, Writing – review & editing. **HongYing Mao:** Methodology, Funding acquisition, Project administration, Supervision, Writing – review & editing.

Declaration of competing interest

The authors declare that they have no known competing financial interests or personal relationships that could have appeared to influence the work reported in this paper.

Acknowledgments

This research was funded by the National Natural Science Foundation of China (Grant No. 22002031, 11504207, 11974307), National Key Research and Development Program (No. 2019YFE0112000) and the Natural Science Foundation of Zhejiang Province (Grant No. LY18F010019, LY19F040005, R21A040006, D19A040001).

Appendix A. Supplementary data

Supplementary data to this article can be found online at <https://doi.org/10.1016/j.carbon.2021.04.022>.

References

- [1] K.S. Novoselov, A.K. Geim, S.V. Morozov, D. Jiang, Y. Zhang, S.V. Dubonos, I.V. Grigorieva, A.A. Firsov, Electric field effect in atomically thin carbon films, *Science* 306 (2004) 666–669.
- [2] A.S. Mayorov, R.V. Gorbachev, S.V. Morozov, L. Britnell, R. Jalil, L.A. Ponomarenko, P. Blake, K.S. Novoselov, K. Watanabe, T. Taniguchi, A.K. Geim, Micrometer-scale ballistic transport in encapsulated graphene at room temperature, *Nano Lett.* 11 (2011) 2396–2399.
- [3] K.S. Novoselov, A.K. Geim, S.V. Morozov, D. Jiang, M.I. Katsnelson, I.V. Grigorieva, S.V. Dubonos, A.A. Firsov, Two-dimensional gas of massless Dirac fermions in graphene, *Nature* 438 (2005) 197–200.
- [4] Y. Zhang, Y.W. Tan, H.L. Stormer, P. Kim, Experimental observation of the quantum Hall effect and berry's phase in graphene, *Nature* 438 (2005) 201–204.
- [5] C. Lee, X. Wei, J.W. Kysar, J. Hone, Measurement of the elastic properties and intrinsic strength of monolayer graphene, *Science* 321 (2008) 385–388.
- [6] A.A. Balandin, S. Ghosh, W. Bao, I. Calizo, D. Teweldebrhan, F. Miao, C.N. Lau, Superior thermal conductivity of single-layer graphene, *Nano Lett.* 8 (2008) 902–907.
- [7] C. Berger, Z.M. Song, T.B. Li, X.B. Li, A.Y. Ogbazghi, R. Feng, Z.T. Dai, A.N. Marchenkov, E.H. Conrad, P.N. First, W.A. de Heer, Ultrathin epitaxial graphite: 2D electron gas properties and a route toward graphene-based nanoelectronics, *J. Phys. Chem. B* 108 (2004) 19912–19916.
- [8] X. Li, W. Cai, J. An, S. Kim, J. Nah, D. Yang, R. Piner, A. Velamakanni, I. Jung, E. Tutuc, S.K. Banerjee, L. Colombo, R.S. Ruoff, Large-area synthesis of high-quality and uniform graphene films on copper foils, *Science* 324 (2009) 1312–1314.
- [9] K.S. Kim, Y. Zhao, H. Jang, S.Y. Lee, J.M. Kim, K.S. Kim, J.H. Ahn, P. Kim, J.Y. Choi, B.H. Hong, Large-scale pattern growth of graphene films for stretchable transparent electrodes, *Nature* 457 (2009) 706–710.
- [10] S. Stankovich, D.A. Dikin, R.D. Piner, K.A. Kohlhaas, A. Kleinhammes, Y. Jia, Y. Wu, S.T. Nguyen, R.S. Ruoff, Synthesis of graphene-based nanosheets via chemical reduction of exfoliated graphite oxide, *Carbon* 45 (2007) 1558–1565.
- [11] S.P. Pan, Y. Hernandez, X.L. Feng, K. Müllen, Graphene as transparent electrode material for organic electronics, *Adv. Mater.* 23 (2011) 2779–2795.
- [12] T.H. Han, Y.B. Lee, M.R. Choi, S.H. Woo, S.H. Bae, B.H. Hong, J.H. Ahn, T.W. Lee, Extremely efficient flexible organic light-emitting diodes with modified graphene anode, *Nat. Photonics* 6 (2012) 105–110.
- [13] J.D. Fowler, M.J. Allen, V.C. Tung, Y. Yang, R.B. Kaner, B.H. Weiller, Practical chemical sensors from chemically derived graphene, *ACS Nano* 2 (2009) 301–306.
- [14] C.H. Lu, H.H. Yang, C.L. Zhu, X. Chen, G.N. Chen, A graphene platform for sensing biomolecules, *Angew. Chem. Int. Ed.* 48 (2009) 4785–4787.
- [15] Y. Huang, J.J. Liang, Y.S. Chen, An overview of the applications of graphene-based materials in supercapacitors, *Small* 8 (2012) 1805–1834.
- [16] J.Q. Liu, L. Cui, D. Losic, Graphene and graphene oxide as new nanocarriers for drug delivery applications, *Acta Biomater.* 9 (2013) 9243–9257.
- [17] S.K. Bae, H.K. Kim, Y.B. Lee, X.F. Xu, J.S. Park, Y. Zheng, J. Balakrishnan, T. Lei, H.R. Kim, Y.I. Song, Y.J. Kim, K.S. Kim, B. Özyilmaz, J.H. Ahn, B.H. Hong, S. Iijima, Roll-to-roll production of 30-inch graphene films for transparent electrodes, *Nat. Nanotechnol.* 5 (2010) 574–578.
- [18] Y. Wang, S.W. Tong, X.F. Xu, B. Özyilmaz, K.P. Loh, Interface engineering of layer-by-layer stacked graphene anodes for high-performance organic solar cells, *Adv. Mater.* 23 (2011) 1514–1518.
- [19] X.J. Wang, G.K. Long, L. Huang, Y.S. Chen, Graphene – a promising material for organic photovoltaic cells, *Adv. Mater.* 23 (2011) 5342–5358.
- [20] L.L. Notte, G.V. Bianco, A.L. Palma, A.D. Carlo, G. Bruno, A. Reale, Sprayed organic photovoltaic cells and mini-modules based on chemical vapor deposited graphene as transparent conductive electrode, *Carbon* 129 (2018) 878–883.
- [21] A.G. Ricciardulli, S. Yang, G.A.H. Wetzelaer, X.L. Feng, P.W.M. Blom, Hybrid silver nanowire and graphene-based solution-processed transparent electrode for organic optoelectronics, *Adv. Funct. Mater.* 28 (2018) 1706010.
- [22] Z.Q. Xu, J. Li, J.P. Yang, P.P. Cheng, J. Zhao, S.T. Lee, Y.Q. Li, J.X. Tang, Enhanced performance in polymer photovoltaic cells with chloroform treated indium tin oxide modification, *Appl. Phys. Lett.* 98 (2011) 253303.
- [23] N. Koch, Organic electronic devices and their functional interfaces, *Chem-PhysChem* 8 (2007) 1438–1455.
- [24] K. Akaike, M.V. Nardi, M. Oehzelt, J. Frisch, A. Opitz, C. Christodoulou, G. Ligorio, P. Beyer, M. Timpel, I. Pis, F. Bondino, K. Moudgil, S. Barlow, S.R. Marder, N. Koch, Effective work function reduction of practical electrodes using an organometallic dimer, *Adv. Mater.* 26 (2016) 2493–2502.
- [25] M. Timpel, H. Li, M.V. Nardi, B. Wegner, J. Frisch, P.J. Hotchkiss, S.R. Marder, S. Barlow, J.L. Brédas, N. Koch, Electrode work function engineering with phosphonic acid monolayers and molecular acceptors: charge redistribution mechanisms, *Adv. Funct. Mater.* 28 (2018) 1704438.

- [26] J.X. Tang, M.K. Fung, C.S. Lee, S.T. Lee, Interface studies of intermediate connectors and their roles in tandem OLEDs, *J. Mater. Chem.* 20 (2010) 2539–2548.
- [27] X.J. Du, W.C. Jiang, Y. Zhang, J.K. Qiu, Y. Zhao, Q.S. Tan, S.Y. Qi, G. Ye, W.F. Zhang, N. Liu, Transparent and stretchable graphene electrode by intercalation doping for epidermal electrophysiology, *ACS Appl. Mater. Interfaces* 12 (2020) 56361–56371.
- [28] M. Kröger, S. Hamwi, J. Meyer, T. Riedl, W. Lowalsky, A. Kahn, Role of the deep-lying electronic states of MoO₃ in the enhancement of hole-injection in organic thin films, *Appl. Phys. Lett.* 95 (2009) 123301.
- [29] M.G. Helander, Z.B. Wang, J. Qiu, M.T. Greiner, D.P. Puzzo, Z.W. Liu, Z.H. Lu, Chlorinated indium tin oxide electrodes with high work function for organic device compatibility, *Science* 332 (2011) 944–947.
- [30] X.M. Zheng, Y.H. Wei, J.X. Liu, S.T. Wang, J. Shi, H. Yang, G. Peng, C.Y. Deng, W. Luo, Y. Zhao, Y.Z. Li, K.L. Sun, W. Wan, H.P. Xie, Y.L. Gao, X.A. Zhang, H. Huang, A homogeneous p-n junction diode by selective doping of few layer MoSe₂ using ultraviolet ozone for high-performance photovoltaic devices, *Nanoscale* 11 (2019) 13469–13476.
- [31] Y.J. Yu, Y. Zhao, S.M. Ryu, L.E. Brus, K.S. Kim, P. Kim, Tuning the graphene work function by electric field effect, *Nano Lett.* 9 (2009) 3430–3434.
- [32] M. Kim, S.J. Lee, H.M. Kim, S.Y. Cho, M.S. Kim, S.H. Kim, K.B. Kim, Highly stable and effective doping of graphene by selective atomic layer deposition of ruthenium, *ACS Appl. Mater. Interfaces* 9 (2017) 701–709.
- [33] S.J. Kwon, T.H. Han, Y.H. Kim, T. Ahmed, H.K. Seo, H. Kim, D.J. Kim, W.T. Xu, B.H. Hong, J.X. Zhu, T.W. Lee, Solution-processed N-type graphene doping for cathode in inverted polymer light-emitting diodes, *ACS Appl. Mater. Interfaces* 10 (2018) 4874–4881.
- [34] W. Chen, S. Chen, D.C. Qi, X.Y. Gao, A.T.S. Wee, Surface transfer P-type doping of epitaxial graphene, *J. Am. Chem. Soc.* 129 (2007) 10418–10422.
- [35] H.Y. Mao, Y.H. Lu, J.D. Lin, S. Zhong, A.T.S. Wee, W. Chen, Manipulating the electronic and chemical properties of graphene via molecular functionalization, *Prog. Surf. Sci.* 88 (2013) 132–159.
- [36] J. Qi, H. Zhang, D.D. Ji, X.D. Fan, L. Cheng, H.X. Liang, H. Li, C.G. Zeng, Z.Y. Zhang, Controlled ambipolar tuning and electronic superlattice fabrication of graphene via optical gating, *Adv. Mater.* 26 (2014) 3735–3740.
- [37] Q.J. Cao, B.Y. Shi, W.D. Dou, J.X. Tang, H.Y. Mao, Background pressure does matter for the growth of graphene single crystal on copper foil: Key role of oxygen partial pressure, *Carbon* 138 (2018) 458–464.
- [38] G. Kresse, J. Furthmüller, Efficiency of ab-initio total energy calculations for metals and semiconductors using a plane-wave basis set, *Comput. Mater. Sci.* 6 (1996) 15–50.
- [39] G. Kresse, D. Joubert, From ultrasoft pseudopotentials to the projector augmented-wave method, *Phys. Rev. B* 59 (1999) 1758–1775.
- [40] J.P. Perdew, K. Burke, M. Ernzerhof, Generalized gradient approximation made simple, *Phys. Rev. Lett.* 77 (1996) 3865–3868.
- [41] S. Grimme, Semiempirical GGA-type density functional constructed with a long-range dispersion correction, *J. Comput. Chem.* 27 (2006) 1787.
- [42] J. Park, W.H. Lee, S. Huh, S.H. Sim, S.B. Kim, K. Cho, B.H. Hong, K.S. Kim, Work-function engineering of graphene electrodes by self-assembled monolayers for high-performance organic field-effect transistors, *J. Phys. Chem. Lett.* 2 (2011) 841–845.
- [43] W. Chen, D.C. Qi, X.Y. Gao, A.T.S. Wee, Surface transfer doping of semiconductors, *Prog. Surf. Sci.* 84 (2009) 279–321.
- [44] R. Meerheim, S. Olthof, M. Hermenau, S. Scholz, A. Petrich, N. Tessler, O. Solomeshch, B. Lussem, M. Riede, K. Leo, Investigation of C₆₀F₃₆ as low-volatility P-dopant in organic optoelectronic devices, *J. Appl. Phys.* 109 (2011) 103102–103106.
- [45] P.O. Gartland, S. Berge, B.J. Slagsvold, Photoelectric work function of a copper single crystal for the (100), (110), (111), and (112) faces, *Phys. Rev.* 28 (1972) 738.
- [46] N. Koch, Energy levels at interfaces between metals and conjugated organic molecules, *J. Phys. Condens. Matter* 20 (2008) 184008.
- [47] H.Y. Mao, R. Wang, J.Q. Zhong, S. Zhong, J.D. Lin, X.Z. Wang, Z.K. Chen, W. Chen, A high work function anode interfacial layer via mild temperature thermal decomposition of a C₆₀F₃₆ thin film on ITO, *J. Mater. Chem. C* 1 (2013) 1491–1499.
- [48] G. van der Laan, C. Westra, C. Haas, G.A. Sawatzky, Satellite structure in photoelectron and auger spectra of copper dihalides, *Phys. Rev. B* 23 (1981) 4369–4380.
- [49] G.G. Totir, G.S. Chottiner, C.L. Gross, D.A. Scherson, XPS studies of the chemical and electrochemical behavior of copper in anhydrous hydrogen fluoride, *J. Electroanal. Chem.* 532 (2002) 151–156.
- [50] D.T. Thieu, M.H. Fawey, H. Bhatia, T. Diemant, V.S.K. Chakravadhanula, R.J. Behm, C. Kübel, M. Fichtner, CuF₂ as reversible cathode for fluoride ion batteries, *Adv. Funct. Mater.* 27 (2017) 170051.
- [51] Y.M. Shi, K.K. Kim, A. Reina, M. Hofmann, L.J. Li, J. Kong, Work function engineering of graphene electrode via chemical doping, *ACS Nano* 4 (2010) 2689–2694.
- [52] K.C. Kwon, K.S. Choi, S.Y. Kim, Increased work function in few-layer graphene sheets via metal chloride doping, *Adv. Funct. Mater.* 22 (2012) 4724–4731.
- [53] M.T. Greiner, L. Chai, M.G. Helander, W.M. Tang, Z.H. Lu, Transition metal oxide work functions: the influence of cation oxidation state and oxygen vacancies, *Adv. Funct. Mater.* 22 (2012) 4557–4568.
- [54] C. Han, J.D. Lin, D. Xiang, C.C. Wang, L. Wang, W. Chen, Improving chemical vapor deposition graphene conductivity using molybdenum trioxide: an *in-situ* field effect transistor study, *Appl. Phys. Lett.* 103 (2013) 263117.
- [55] R. Gholizadeh, Y.X. Yu, Work function of pristine and heteroatom-doped graphenes under different external electric fields: an ab initio DFT study, *J. Phys. Chem. C* 118 (2014) 28274–28282.
- [56] M.C. Biesinger, L.W.M. Lau, A.R. Gerson, R. St. C. Smart, The role of the auger parameter in XPS studies of nickel metal, halides and oxides, *Phys. Chem. Chem. Phys.* 14 (2012) 2434–2442.